Low energy electron transmission through layered materials and chiral organic films

Neu, P.S.

6 PHOTOEMISSION FROM CHIRAL MOLECULE FILMS

6.1 Introduction

The Chirality-Induced Spin Selectivity (CISS) effect has been investigated for both its fundamental implications and its promising applications since the first report in 1999 [1]. This first study reported an asymmetry in spin population for electrons photoemitted from films of stearoyl lysine, a chiral organic molecule. The effect is intriguing, as the degree of spin polarization found cannot be quantitatively explained by spin-orbit coupling. Calculations based on spin-orbit coupling yield a 100-1000 times lower degree of spin polarization than found in experiments [2], due to the small spin-orbit coupling parameters of the lightweight (carbon-) atoms involved. Recent studies attempt to explain the CISS effect as intrinsically related to disorder that diminishes at low temperatures [3] or by spin-dependent coherent scattering [4].

The first set of experiments by Ray et al. [1] focused on films of lefthanded (L) and righthanded (D) stearoyl lysine, five monolayers thick, and the effect of the composition of the layers on spin-selectivity. They measured the (energy-dependent) photoemission intensity from five layers of L- stearoyl lysine under illumination with left- and right-circularly polarized light (reprinted in Fig. 6.1a). They interpreted the difference in photoemissivity between left- and right-circularly polarized light as a spin-filtering effect on the electrons photoemitted from the gold substrate, which have a preferred spin depending on the handedness of the light.

Furthermore, they found that in a stack of organic films of different handedness the degree of spin polarization was only dependent on the number of layers of each handedness and not their order. The authors concluded that the organic layers act as independent spin filters with a certain spin-dependent transmission probability. For five monolayers consisting of 99% L-stearoyl lysine and 1% R-stearoyl lysine, they reported the absence of the intensity-dependence on the handedness of light (Fig. 6.1a, panel B), suggesting that spin-selectivity is a collective phenomenon in the layer.

In a later photoemission experiment, Göhler et al. [5] reported on the spin polarization of photoelectrons emitted from monolayers of DNA. They show that the spin polarization differs by a few percent between left- and right-circular polarized illumination (Fig. 6.1c), which is attributed to the spin-asymmetry in photoemission from the underlying gold. However, the CISS effect was strong enough to keep the same majority spin anti-parallel to the direction of travel, independent of laser light polarization (see Fig. 6.1c). Also, they found a difference in photoemission intensity depending on the handedness of the laser light, as reprinted in Figure 6.1b, in line with the spin-filtering effect reported previously by Ray et al. (Fig 1a).

For DNA of different lengths, Göhler et al. [5] found a spin polarization of 31% for 50 base pairs, rising to 57% (anti-parallel to the direction of travel for all lengths) for 78 base pairs of double-stranded DNA (under illumination with linearly polarized light).

Scanning probe measurements of CISS report a large site-dependence of the degree of spin-polarization [6,7]. Although the assembly of organic film aims for uniformity, one can expect the formation of defects and domains of molecules (with the same orientation), possibly producing hotspots in photoemissivity and spin selectivity.

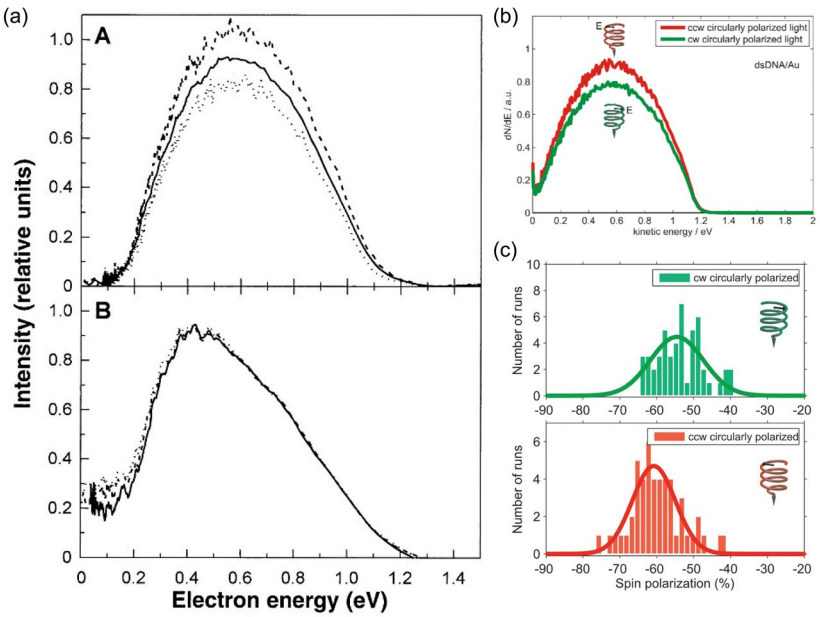

Figure 6.1: Exemplary reports of chirality-induced spin selectivity (CISS) and the accompanying intensity difference between right- and left-circularly polarized light measured in photoemission experiments. (a) Reprint of Figure 2 from Ray et al. [1] showing the electron energy distribution obtained with linearly polarized light (solid line), right-handed circularly polarized light (dashed lines), and left- handed circularly polarized light (dotted lines). The film consisted of five layers of enantiopure L-stearoyl lysine (A) and a mixture with 1% D-stearoyl lysine added (B). (b, c) Reprint of Fig. S6 and Fig. 3 from Göhler et al. [5] showing the photoemissivity intensity (b) and spin polarization (c) of double stranded DNA for right-circularly polarized light (green) and left-circularly polarized light (red). The interpretation is that chiral molecular layers act as spin filters with different transmission probabilities for the different spins emitted from the gold substrates, i.e. CISS. Reprinted with permission from AAAS.

In our experiment, we set out to use the imaging capabilities of the ESCHER setup, to acquire an image of the polarization-dependent photoemission. As we have no means of measuring spin directly in our ESCHER setup, we instead control the handedness of light and image the resulting photoemission intensity. The experiments by Ray et al. [1] and Göhler et al. [5] show that spin-selectivity goes hand in hand with the photoemission intensity dependent on handedness of light (see Fig. 6.1). The reported effect on intensity is in the order of ± 10 % compared to the photoemission intensity under linearly polarized illumination.

We will study a sample of sulfur-functionalized R-BINAP molecules (2,2′-bis(diphenylphosphino)-1,1′-binaphthyl) on top of a 40 nm gold layer. The layered sample structure mimics the one in the photoemission experiments cited above. BINAP is a short, carbon-based molecule with a chiral center in the middle, and is commercially used for chiral synthesis. Recent studies report conductive-AFM measurements of the CISS effect in BINAP and a corresponding asymmetry in circular-dichroism over a broad DUV wavelength range [8]. As the thin chiral molecular film is prepared on top of a non-chiral layer, we will first explore the photoemission of a non-chiral substrate. To gain further understanding of the polarization control setup, we also investigate the polarization-dependent photoemission of gold

nanostructures with sizes in the order of the deep ultraviolet (DUV) wavelength. Finally, we report on the photoemission of a thin film of chiral R-BINAP molecules [9], and its dependence on the circular/elliptical polarization of the (DUV) light.

6.2 Experimental

6.2.1 Linear polarization and photoemission

In the ESCHER LEEM setup, the DUV laser beam (224 nm, HeAg70, PhotonSystems) enters the vacuum chamber through one of the fused silica viewports directed toward the sample. Unlike in the geometry used in the group of Zacharias [5,10], the light in our experiment does not hit the sample perpendicular to the surface, but under an angle of $\Theta = 70°$ from the surface normal. Thus, the incoming and reflected light rays span a plane, with different reflectivities for the linear polarization perpendicular to the plane (s polarization) and the linear polarization parallel to the plane (p polarization). The geometry of the light ray incident on the sample, together with the s and p polarization electric field components E_s and E_p, is shown in Figure 6.2. The angle enclosed by the ray and the sample is $\alpha = 20°$.

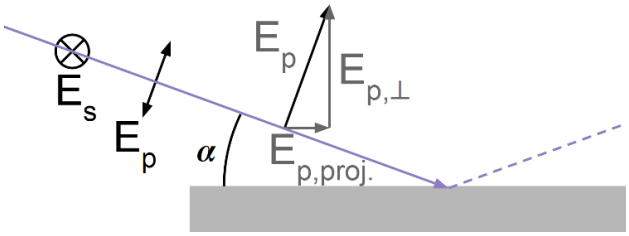

Figure 6.2: Sketch of the illumination geometry in our experiment. The DUV laser beam (violet) is incident on the sample (grey) under a sharp angle given by the setup of the vacuum chamber. Linear components of the electric field of the DUV light ray and electric fields projected on the sample are shown. The s component does not change when it is projected, as it is always perpendicular to the plane spanned by the incident and reflected light ray. The p component of the electric field is diminished when incident on the sample, with $E_{\mathrm{p,proj.}} = \sin(\alpha) \cdot E_{\mathrm{p}}$.

While usually the effect of linear polarization direction on light reflection (and for dielectrics transmission) is discussed, it will also have an influence on the photoemission from a non-transparent surface. In general, the photoemission intensity will depend on the band transitions in the material, which are the contrast mechanism in (polarization-dependent) ARPES of crystalline surfaces. For the gold and silicon surfaces one can expect a simple relation: The photoemission is proportional to the light that is not reflected, i.e., absorbed (assuming a bulk sample).

According to the Fresnel equations [11], the reflection coefficients of light, on the vacuum-sample interface with the complex refractive index n of the sample, are

$$R_s = \left| \frac{\cos\Theta - \sqrt{n^2 - \sin^2\Theta}}{\cos\Theta + \sqrt{n^2 - \sin^2\Theta}} \right|^2$$

and

$$R_p = \left| \frac{\mathrm{n}^2 \cos\Theta - \sqrt{n^2 - \sin^2\Theta}}{\mathrm{n}^2 \cos\Theta + \sqrt{n^2 - \sin^2\Theta}} \right|^2$$

for s and p polarized light, respectively, and the angle $\Theta = 90° - \alpha$ off the surface normal. Thus, the absorbed intensities are $T_{s/p} = 1 - R_{s/p}$.

At 224 nm wavelength and $\Theta = 70°$, we can expect $T_s = 0.44$ and $T_p = 0.88$ for silicon according to the refractive index reported by Aspnes and Studna [12] and expect $T_s = 0.32$ and $T_p = 0.81$ for gold (Au) according to Ciesielski et al. [13], who measured a 35 nm thin Au film on SiO_2.

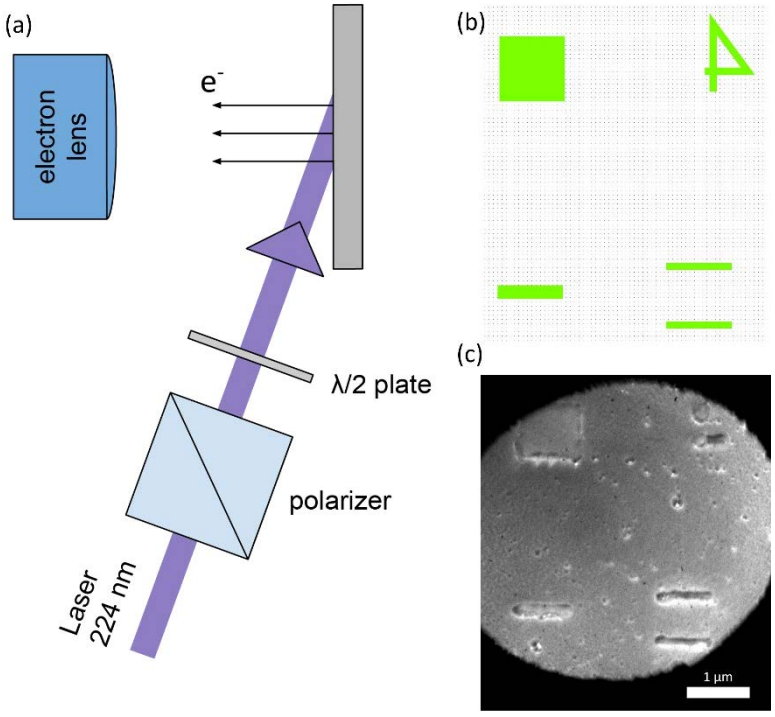

Figure 6.3: (a) The linear polarization is controlled by a polarizer (Glan-Taylor prism) and a $\lambda/2$ plate on a motorized rotation mount outside the vacuum chamber. The sample was patterned electron-beam lithographically according to the design in (b). The LEEM image (c) at the mirror mode transition shows, that the square and lines transferred successfully, while the number 4 only shows up in a dot and a line. The raised features are made of 40 nm gold on top of a 5 nm titanium sticking layer.

The polarization control, which is attached to the outside of the vacuum viewport flange, (Fig. 6.2a) consists of a linear polarizer (Glan Taylor style prism, Thorlabs GLB10) and a $\lambda/2$ plate (Tim optics Jena) that is rotated by a stepper motor. The laser beam is aligned onto the sample with a mirror (aluminum, DUV-enhanced mirror, Edmund optics). The mirror already introduces a partial polarization of the laser beam, due to the Fresnel equations explained earlier. The linear polarizer is kept constant during the data acquisition, as to not vary the intensity due to varying the mirror and linear polarizer axis, and the linear polarization direction is varied with the $\lambda/2$ plate. We name the angle between the linear polarizer and the $\lambda/2$ plate Φ.

Turning the $\lambda/2$ plate with respect to the linear polarizer leads to a doubling ($2 \cdot \Phi$) of the polarization vector angle with respect to the lambda half plate fast (slow) axis. Aligning either the fast or slow $\lambda/2$ plate axis with the linear polarizer, which happens every $90°$, leads to an unchanged polarization. Therefore, the polarization vector after the $\lambda/2$ plate, i.e., incident on the sample, is $90°$ periodic in $\lambda/2$ plate angle.

To align the linear polarizer to the s polarization axis on the sample, we rotate the $\lambda/2$ plate and find the angle of minimum photoemission. Then we set the linear polarizer to double the angle where that minimum was found, as the angle was doubled by the $\lambda/2$ plate. The setting of the linear polarizer is then checked by rotating the $\lambda/2$ plate symmetrically around the new $\Phi = 0°$ axis of the linear polarizer.

6.2.2 Principal tests on gold structures

To test our set-up, we first use samples that consist of a lithographically defined gold (40 nm, on 5 nm chromium) pattern (Fig. 6.3b). We acquired a LEEM image at the mirror mode transition energy and with a contrast aperture inserted (Fig. 6.3c). The size of the gold square is approximately 1 µm x 1 µm and the size of the lines is approximately 1 µm x 150 nm according to the LEEM image. The electron beam lithography design contained smaller structures, with four times smaller base lengths as indicated by the 4 in Figure 6.3b, which could not be found in PEEM (with the 224 nm laser or the Hg light source) or LEEM. Small structures are known to not be exposed correctly or not adhere to the substrate during the removal of the excess gold (lift-off). Alike, the number 4 in the design was too small to transfer fully, as seen in the LEEM image Figure 6.3c. The size of 1 um of the smallest structures produced and shown in Figure 6.3c is still comparable to 4 times the wavelength of the light used and the short dimension of the lines is smaller than the wavelength, thus can be expected to show plasmonic behavior. The lines have a characteristic aspect ratio of $1000\ \text{nm}/150\ \text{nm} \approx 6.7$.

The data in Figure 6.4 is acquired by rotating the $\lambda/2$ plate angle in steps of $360°/64 \approx 5.6°$and integrating the image over 256 laser pulses. The integrated image is shown in the inset of Figure 6.4, with the arrow colors corresponding to the plot. First, we note that all curves in Fig. 6.4 are indeed $90°$ periodic. The substrate photoemission curve, which was used to align the linear polarizer to the s polarization and define the Φ angle, has a minimum at $0°$, by construction, and at multiples of $90°$. The photoemission curve of the gold square (orange, Figure 6.4) follows the same sine-like curve, but at approximately 5 times higher intensity. Photoemission from gold is indeed expected, as the work function of gold is 5.10 – 5.47 eV according to literature [14,15] (depending on facet, crystallinity, etc.), which is lower than the photon energy of 5.54 eV at 224 nm wavelength. Although the work functions of the (p-doped) Si and its native silicon oxide layer are lower than that of gold, around 5.0 eV [16], the Si substrate emits fewer photoelectrons than the gold. We attribute this to the lowering of the gold work function due to organic contaminations deposited during the dissolution of PMMA in acetone. Organic contamination of Au is known to further lower the work function by up to 1 eV [17].

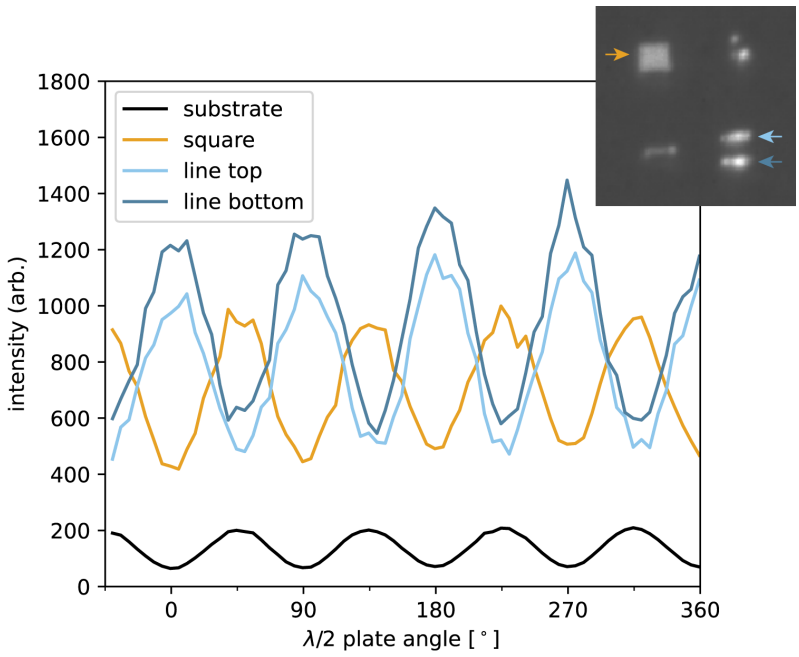

Figure 6.4: Photoemission intensity as function of $\lambda/2$ plate angle for the features indicated in the inset. The inset shows the integrated photoemission image. The dependence of photoemission on linear polarization direction is expected as the light is incident on the surface under a sharp angle, leading to polarization-dependent reflection. All curves are 90° periodic in $\lambda/2$ plate angle, as this is the periodicity of going from p-polarized to s-polarized to p-polarized linear light. The photoemissivity curve of the square is in phase with the one of the substrate, while the ones of the lines are shifted by 45°, pointing to a plasmonic response. Here, the maximum of photoemission occurs when the light is polarized parallel to the long direction of the lines.

The photoemission of the two gold lines (marked in blue in Figure 6.4) is shifted by 45° in $\lambda/2$ plate coordinates/angle with respect to the gold square (and substrate) photoemission curve. As a check, we moved the sample stage along the direction of the lines, to move the stage by a visible amount to determine the orientation of the lines with respect to the polarizer. As far as can be judged by eye, the lines are perpendicular to the linear polarizer orientation. Thus, the photoemission maxima at $\Phi = 45°$ in $\lambda/2$ plate correspond to polarization parallel to the lines. This is in line with the results reported by Sun et al. [18], where two photoemission hotspots at the ends of the gold structures parallel the laser polarization were observed.

As argued above, the photoemission intensity is expected to follow a sine function, as the polarization rotated by 2Φ with respect to the original s-polarization, is projected onto the s- and p-component. Figure 6.5 shows the function

$$\frac{I(\Phi)}{I_0} = 1 + \left(T_p/T_s - 1\right) \cdot \sin^2(2\Phi + \Phi_0) \qquad \text{eq. 1}$$

overlaid on the data. For the lines, a phase shift $\Phi_0 = 45°$ is applied, as they are out of phase as discussed above, whereas no phase shift ($\Phi_0 = 0°$) is applied to the substrate or gold square. The only free parameter in the model is the intensity I_0. The relative intensity of maxima and

minima is not fitted but set by the ratio $T_p/T_s = 0.81/0.32$ (0.88/0.44 for the Si substrate) calculated from the literature refractive indices.

The data in Figure 6.5 is described well by the sine behavior in Equation 1 for $I(\Phi)$. The photoemissivity of both the line and square gold structures matches the contrast between s and p polarized expected from literature. This in turn confirms that the photoemission is proportional to the non-reflected intensity, as determined by the Fresnel equations. The phase shift Φ_0 of the line structures is close to 45°, although that is a coincidence in how the sample was oriented. Had the sample been rotated by another 90° during mounting, then the lines would have been parallel to the s polarization direction and thus not show a phase shift. The relative difference between the maxima and minima of the substrate is slightly larger than expected for Si, which can be the result using p-doped Si, that is more conductive than undoped Si.

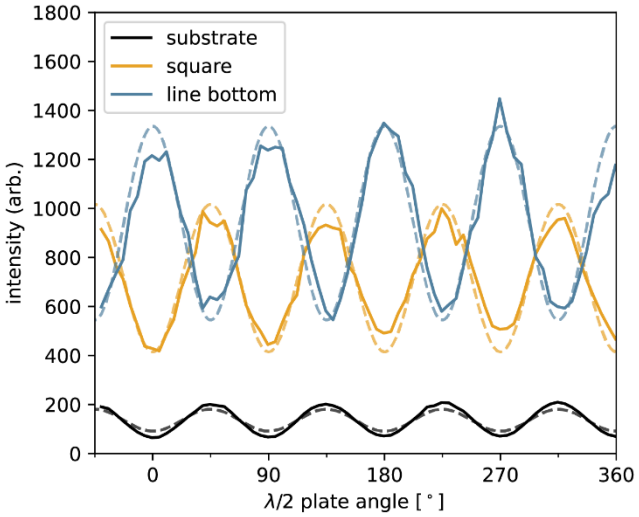

Figure 6.5: Photoemission intensity data (solid lines) and sine function fit according to Eq. 1 (dashed lines). The relative amplitude of the sine, i.e., the ratio of maximum to minimum, is fixed to the calculated value of T_p/T_s according to literature, $T_p/T_s = 0.81/0.32$ for gold and $T_p/T_s = 0.88/0.44$ for the Si substrate. The scaling factor of the sine is fitted, and the angular offset is set to 0° (for the substrate and 'square' curves) or 45° (for the 'line bottom' curve). The good correspondence with this one parameter fit shows, that the photoemission is proportional to the intensity of light not reflected according to the Fresnel equations.

6.2.3 Polarization-dependent Photoemission from BINAP

Molecules based on 2,2′-bis(diphenylphosphino)-1,1′-binaphthyl (BINAP) are commonly used as enantiopure precursors/catalysts for the enantiomer-specific synthesis of molecules. BINAP is commercially available in high enantiopurity. The S-functionalized short BINAP molecule used in this chapter was provided by our collaborators C. Hsu, A. Philip and F. Grozema at the Faculty of Applied Sciences, Delft University. The same molecule has been studied in fast break junction experiments described in chapter 7 of the PhD thesis of Chunwei Hsu [19].

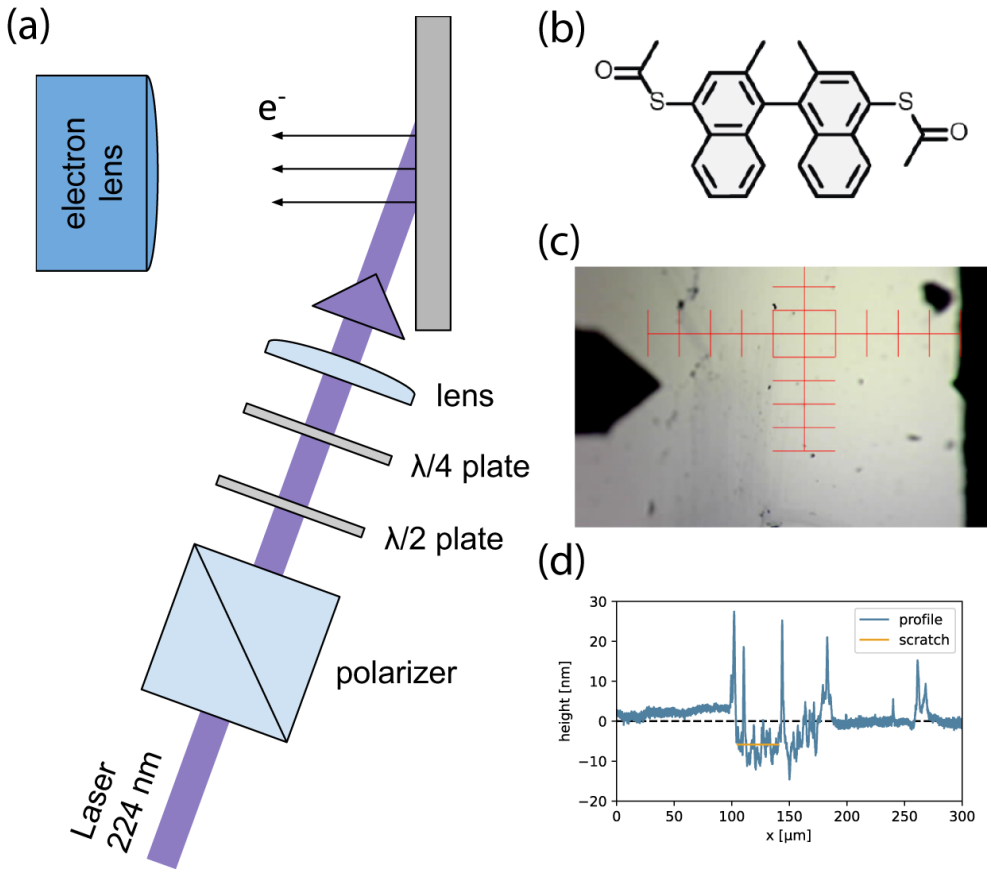

Figure 6.6: Optical setup (a) for elliptical polarization generation used on the chiral molecules. Compared to the linear polarization experiment (Fig. 6.3a), a $\lambda/4$ plate is added after the rotatable $\lambda/2$ plate, to turn the linear polarization into elliptical polarization. Also, a lens (focal length f=175 mm) is added, to focus the DUV laser beam and thus increase the flux of photons and proportionally photoemitted electrons. The BINAP molecule is sketched in Figure 6.3b. The height of the BINAP film on gold is measured with the profilometer, by scratching the surface with a carbon tweezer tip and measuring the depth of the created trench. The optical image (c) with the vertical scratch (between the black tip and the red crosshairs) and the measured height profile (d) are shown. The scratch (marked orange in the profile, d), removing the molecular layer and possibly some of the gold layer, is 5 nm deep. The molecule structure (b) is a reproduction of Figure 7.6 in [19], where the same molecules were used.

For sample preparation, a 20 nm gold film was evaporated on a Si chip with a 5 nm titanium sticking layer. Then the modified BINAP molecules were deposited on the coated chip, by incubating it in a 0.1 mM BINAP (in dichloromethane, DCM) solution for 24 hours. On the next day, the chip was rinsed in DCM and blow-dried in nitrogen to remove excess BINAP molecules. We scratched the sample with a carbon tweezer tip to remove a strip of molecules and create an achiral reference area. Profilometer profiles were acquired after the in-vacuum measurement. The roughness of the layer shows, that it is not a well-assembled monolayer (shown in Figure 6.6d). Still the profile linecut across this scratched trench, that scratched down into the gold layer, shows that the BINAP film is thinner than 5 nm high.

To measure photoemission depending on the handedness of the circularly polarized light, a $\lambda/4$ plate was added to the polarization control optics. The optical setup for this experiment is shown in Figure 6.6a. If the linear polarized light is incident at $\pm 45°$ from the fast axis of the $\lambda/4$ plate, the resulting light will be right-/left- polarized. If the linear polarized light is incident along the fast (or slow) axis of the $\lambda/4$ plate, the polarization will remain linear. In between these prototypical settings, any elliptical polarization is possible. We note that the axes of the ellipse always coincide with the fast and slow axes of the $\lambda/4$ plate, unlike what many illustrations in textbooks suggest [20,21]. Therefore, we will keep the $\lambda/4$ plate fixed in our experiment, aligned parallel to the linear polarizer, and vary the resulting polarization by rotating the $\lambda/2$ plate angle Φ on a motorized mount. Rotating the $\lambda/4$ plate would result in a rotation of the long axis of the ellipse with respect to the s-/p-polarization axis. If the $\lambda/4$ plate is indeed perfectly aligned parallel to the s-/p- axis of the sample and if it were rotated symmetrically, the linear projection of the long ellipse axis on the s-/p-axis would not affect the photoemission intensity background, but as we expect the chirality signal to be small compared to the linear polarization response (investigated above), fixing the $\lambda/4$ plate is advantageous.

We checked the alignment of the $\lambda/4$ plate by symmetrically rotating the $\lambda/2$ plate and comparing the photoemission intensity on an achiral area of the sample. The achiral area was produced by illuminating it with the LEEM beam at 100 eV electron energy for 30 s, which leads to bond breaking and making [22]. A loss of the chiral signal has been shown in transport devices after applying 1 mA current over a 5 x 5 μm^2 junction [23] and by ellipsometry after exposure to UV light [24].

As the light is incident on the sample under an angle of $\Theta = 70°$ from the surface normal, the projection of circular polarization on the sample will be squished into elliptical polarization along the plane spanned by the incident and reflected ray, while the polarization component perpendicular to that plane (s-component) remains unaltered. The projected component $E_{\mathrm{p,proj.}}$ of the polarization E_{p} is shortened to $E_{\mathrm{p,proj.}} = \sin(\alpha) \cdot E_{\mathrm{p}} \approx 0.34 \cdot E_{\mathrm{p}}$ as shown in Figure 6.2. To compensate for this projection effect and reach a circular polarization projected on the sample, we aim to adjust the laser polarization to elliptical polarization that is elongated by $1/\sin\alpha$ in the p-polarization direction. The ellipticity of the light after passing the $\lambda/4$ plate is given by the ratio of the linear electric field projected on the fast and slow axis of the $\lambda/4$ plate, $E_{\mathrm{fast}}/E_{\mathrm{slow}} = E_{\mathrm{lin.}} \cdot \cos(2\Phi)/\sin(2\Phi)$. Thus, the requirement is $\tan(2\Phi) = \sin(\alpha)$. This is the case for the fast axis of the $\lambda/4$ plate aligned to the p-polarization direction and the linear polarized light incident on the $\lambda/4$ plate at $2\Phi = \pm 18°$ from the fast axis. Therefore, we will acquire images with the $\lambda/2$ plate set to $\Phi = \pm 9°$ from the fast axis of the $\lambda/4$ plate. For short, we will refer to these settings as R-polarized ($\Phi = +9°$) and L-polarized ($\Phi = -9°$) light.

For the following measurement, we also added a lens (DUV enhanced, plano-convex, f=175 mm) to the setup, to focus the laser intensity to a smaller spot and thus increase the flux of photoemitted electrons. The focused spot is still larger than the field of view in PEEM mode. As the focal length of the lens is large with f = 175 mm, the distortions it introduces to

polarization are expected to be minimal. As the electron emission is still low and the low electron count will be the major noise source, a large field of view was chosen in the recording.

The horizontal lines in Figure 6.6 are the scratch marks created by scratching the carbon tweezer tip over the sample to remove the molecules. The darker photoemission indicates that we reached a more pristine gold layer that has a higher work function than the BINAP molecules.

To test the effect of the different elliptical polarization on electron emission, thus the CISS effect on the BINAP film, the difference image between the right-handed and left-handed illumination images (Fig. 6.7b and Fig. 6.7a, respectively) is shown in Figure 6.8a. The scale bar shows the relative difference between R and L polarization, with areas that are brighter in right-handed polarization in red and areas that are brighter in left-handed polarization in blue. Zero difference, i.e., no chiral effect, is shown in white. The difference image in Figure 6.8a is very noisy and does not allow us to identify a clear trend. However, this may be due to the fact that we start with noisy images (due to low electron count) already. To reduce the noise in the difference image further, we will need more images.

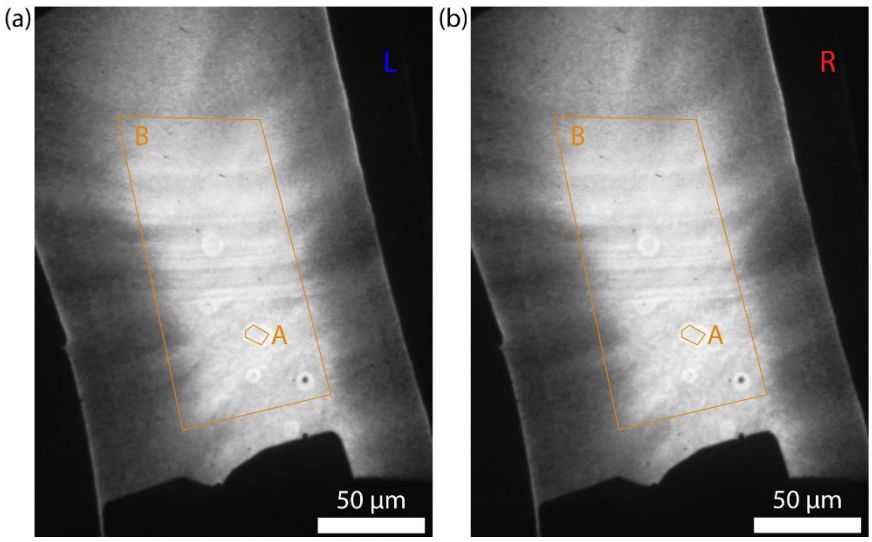

Figure 6.7: Photoemission microscopy images acquired with (a) left elliptical polarized (labelled L) light and (b) right elliptical polarized light (labelled R). Each image is integrated over 64 laser pulses, and no clear difference between L- and R-polarization is visible. Area A marks the area that is expected to be achiral, as it was illuminated with the electron beam at 100 eV for 30 s. Area B is taken as a large reference area. The intensity histograms of area A and B will be discussed in Figure 6.8d.

Figure 6.7 shows photoemission images of the sample acquired by illuminating the sample with left-polarized light (labeled L, Fig. 6.7a) and with right-polarized light (labeled R, Fig. 6.7b). Each image was acquired by integrating 64 laser pulses. There is no clear difference visible between the two images. The electron beam imprint, created by exposing the sample to 100 eV electrons for 30 seconds, is labeled area A in Figure 6.7a/b. It appears as a bright, elongated imprint, and was used to align the optical retardation plates symmetrically, as we assume that the chirality of the molecules has been destroyed. Some other bright spots with a dark spot in

the center are visible; these are not beam imprints, but bubbles formed during drying of the sample.

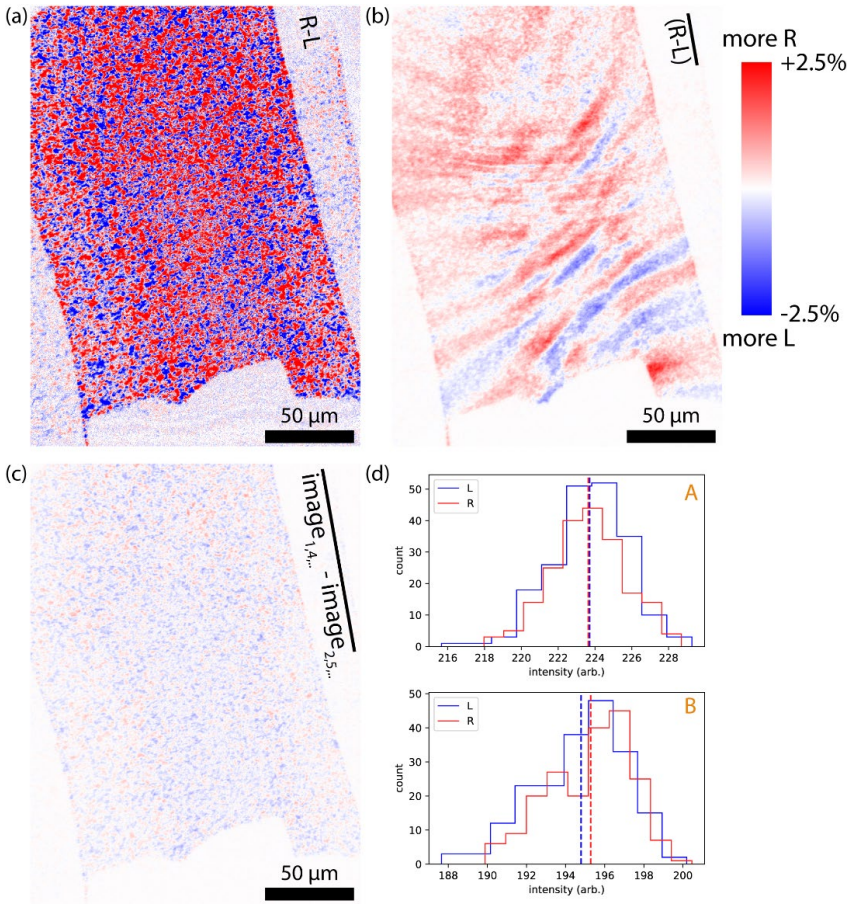

Figure 6.8: (a) Difference image between one left elliptical polarized and one right elliptical polarized image, showing mostly noise as the intensity in each image is low. (b) Difference between all 200 left elliptical polarized images and all 200 right elliptical polarized images, showing characteristic streaks of areas that are more emissive in R-polarization and areas that are more emissive in L-polarization. These large, smoothly transitioning areas do not coincide with the sharp features, like the achiral beam damage spot or the scratch, on the sample, indicating that the emissivity difference is related to uneven illumination depending on $\boldsymbol{\lambda/2}$ plate setting. (c) Difference between 132 images in steps of 3, and their following images, thus image 1,4,7,.. minus image 2,5,8,… . Thus, there are 66 right-elliptical and 66 left-elliptical images in each group, thus polarization effects should even out, as we see in the noisy image. (d) Photoemission intensity histograms, separate for right- and left-handed elliptical light (L and R), for the areas indicated in Figure 6.7. Area A is a beam imprint used for aligning the polarization symmetrically and area B a large average.

Hence, we recorded 200 left-polarized and 200 right-polarized images like in Figure 6.7, illuminated with 64 laser pulses each, always alternating between L and R polarization after 64 laser pulses, as to minimize the effect of laser intensity drift and sample deterioration over the acquisition period of approximately 3 hours. The difference image between these 200 left-polarized and 200 right-polarized images is shown in Figure 6.8b. This image is less noisy indeed and features patches of more photoemissivity at right-handed or left-handed polarization, with relative intensity differences of up to 2.5 %.

However, these areas mostly have very smooth transitions, like continuous hills and valleys, that do not coincide with the features on the sample visible in Figure 6.7. For CISS features, we would expect a sharp loss of contrast at the non-chiral, i.e., the scratched and electron beam-burnt, areas. Only the sharp edges of the horizontal scratches are visible as white lines in Figure 6.8b, but there is no difference between the scratched area and the surrounding molecules. The beam imprint used for aligning polarization falls between a R-dominated and a L-dominated area.

The fact that the difference image has little coincidence with the features of the sample, suggests that the polarization difference in different areas is caused by different intensity distribution of the incoming light when changing the $\lambda/2$ plate setting. To test that the difference between images shown in Figure 6.8b is a result of the different polarizations, instead of different intensities, we next regroup the images and take the difference between equally many right-polarized and left-polarized images. The difference image is shown in Figure 6.8c. Here, we have grouped images 1,4,7,… together, thus 66 right and 66 left circularly polarized images grouped together, minus images 2,5,8,… , thus again 66 right and 66 left circularly polarized images, grouped together. The fact that the resulting difference image only contains noise around zero shows, that the difference in Figure 6.8b is related to the different polarization settings.

The mean intensity of the beam imprint area A was extracted for each of the 200 left-polarized and 200 right-polarized images and makes up the histograms shown in Figure 6.8d, separated for left (L, blue) and right (R, red) circular polarization. The mean of the R- and L-polarized histogram is shown with a dashed line in the respective color. In area A, the mean intensity of the R- and L-polarized photoemissions coincides, which is not surprising as we used this area to align the polarization symmetrically.

The histogram acquired in the same way on the big, illuminated area, labeled B in Figure 6.7, is also shown in Figure 6.8d. The shift towards higher intensity of the histogram in R-polarized illumination suggests that photoemission is favored in R-polarization. The mean intensity of area B in R-polarization is approximately 1% higher than in L-polarization. However, from the different L- and R-polarization favored patches in the integrated difference image Fig. 6.8b, we conclude that this majority is ambiguous, as we could have chosen a different spot than area A to align the polarization symmetrically and would have gotten a different result.

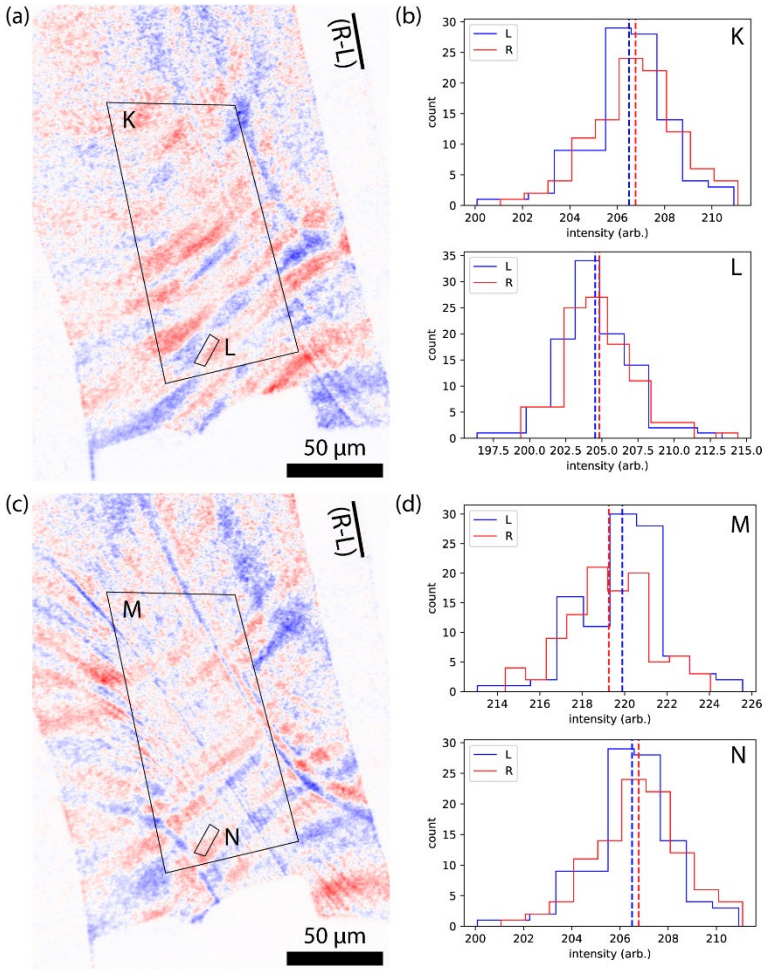

Figure 6.9: More difference images (a,c) of different areas and their histograms (b,d) on the respective large areas (K, M) and the beam imprint areas (L, N). The difference images (a,c) were acquired like the one on Figure 6.8b, but on different areas. The images show areas around the vertical tweezer tip scratch. The streaks caused by uneven illumination in L- and R-polarization show the same pattern for all the areas, confirming that they are unrelated to the chiral molecules on the sample. Depending on the chosen area, one may get a preference for photoemission in L- or R-polarization, as visible in the histograms (b,d). The electron beam spots (L,N) are shifted with respect to Figure 6.7, as the sample was moved, deflecting the electron beam.

The integrated difference images from another two areas (100 R-polarized minus 100 L-polarized images each) are shown in Figure 6.9a/c, together with their corresponding histograms in Figure 6.9b/d, respectively. Both difference images show the same horizontal streak pattern, which we attributed to uneven illumination in Figure 6.8. The difference image in Figure 6.9c shows an area closer to the edge of the sample. The histograms in Figure 6.9 are acquired on the large illuminated areas K/M (like area B in Figure 6.7) and the beam imprint areas L/N (comparable to area A in Figure 6.7). The real-space position of the beam imprint area is shifted in comparison to Figure 6.7 because of the non-perpendicular electric field lines close to the edge of the sample. The area K in Figure 6.9a shows a slight preference for photoemission from R-polarized light, while the area M in Figure 6.9c is brighter in L-polarized light. Still, both these differences lie within 0.5 %. The difference in the small beam imprint

areas (K, M) is not zero anymore, as the electron beam is shifted due to moving the sample and the same polarizer angles as in the previous images have been used.

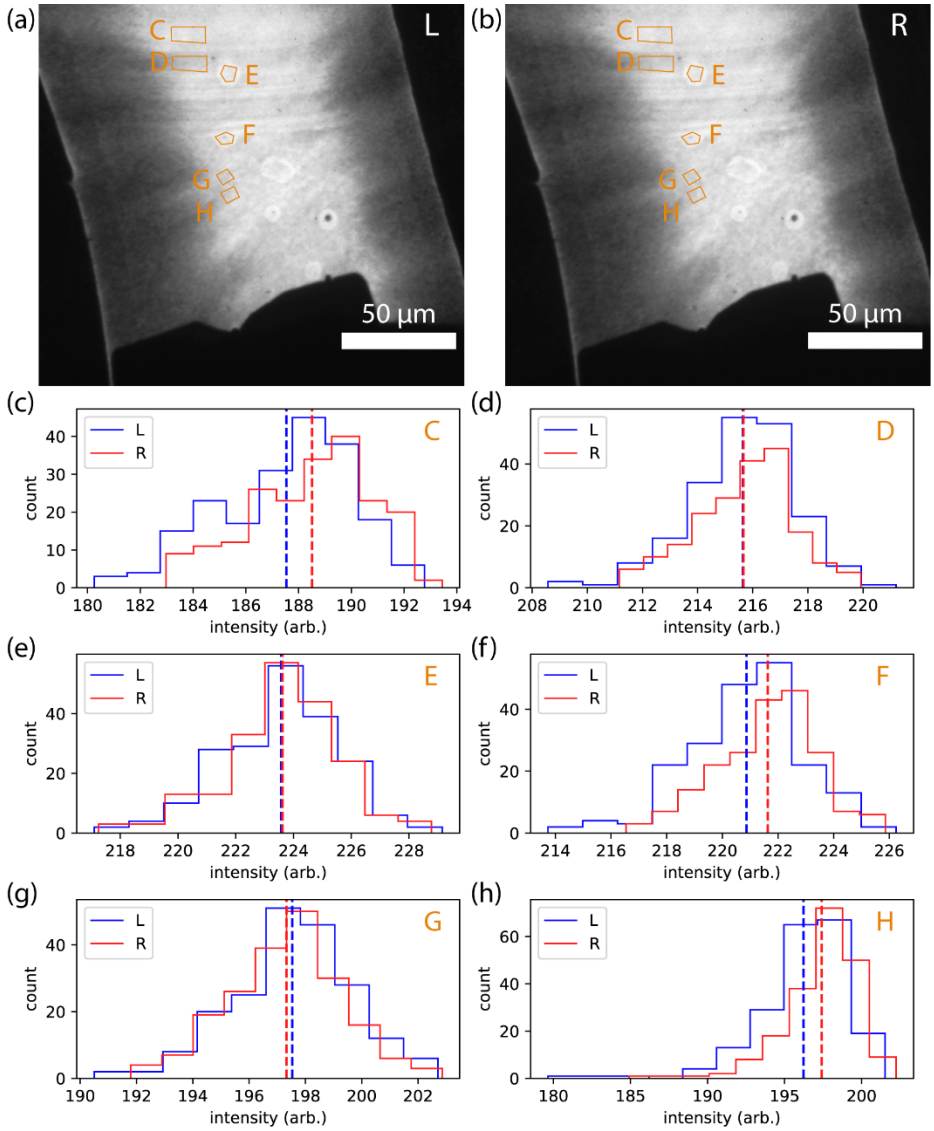

Figure 6.10: Intensity histograms (c-h) on more areas with specific features indicated in the L-polarization (a) and R- polarization (b) images. In area C, the molecules were scratched off with carbon tweezers, whereas area D next to the layer was left untouched. Areas E and F show bubbles that formed during incubation of the sample. G and H have no apparent different morphology in the photoemission images a/b. However, they happen to be illuminated with different intensity in the right- and left-elliptical polarization setting.

The polarization-dependent histograms of more features that we pointed out in Figure 6.8 are shown in Figure 6.10. The areas labeled in Figure 6.10a/b are the horizontal scratch (D) and a neighboring area (C), a beam imprint (E), a bubble F, and two neighboring areas that are not separated by a visible feature (G and H). Areas G and H have been chosen, as they look like parts of the same uniform area in the photoemission images but fall on streaks of different majority polarization emission in the difference image (Fig. 6.8b).

The histograms of the different areas, shown in Figure 6.10c-h, show how the photoemission intensity varies over the sample in real space: From favoring L-polarization in area G, over no chiral asymmetry in areas D and E, to favoring R-polarization in the other 3 areas. We note again that we attribute the handedness-asymmetry to the differences in illumination, although one could arrive at a different conclusion by looking at each of the individual histograms. Especially the difference between histograms of areas G and H, which cannot be explained by differences in the sample, evokes suspicion.

In all cases, the differences between the mean intensity of left-handed and right-handed induced photoemission we measured are below 1% for each area considered.

6.2.4 Further calculation of transmitted polarization

Still, our conclusion above needs some refinement. In an experimental geometry with normal incidence of the light, the phase shift of the reflected light does not change light polarization due to symmetry, as s- and p-polarization are equivalent/undefined. The larger the incidence angle (from the normal) is, the larger the phase shift difference between the s- and p-polarization [25]. While the photoemission experiments by Ray et al. [1] were conducted with the UV light at normal incidence on the sample, in our case the laser beam hits the sample at 70° from the surface normal. We expect that most electron microscopy setups will suffer from similar constraints, as it is crucial to have the electron objective lens aligned straight over the sample, thus obstructing the normal light path.

Although we chose the incident light polarization in our experiments such that its projection on the surface yields circularly polarized light, we will now also discuss the polarization of the transmitted light after taking the phase shift upon transmission through a metal into account. We expect that the transmitted polarization, i.e., right below the gold surface, is decisive for the polarization-dependent spin-polarized photoemission from gold.

For this reason, we calculated the reflected polarization from the incident elliptical polarization as applied in our experiment above, using the complex refractive index reported in [13]. The sum of the incident and reflected field are shown in Figure 6.11. The blue curve shows the path the electric field vector described as it is propagated in time. As the $\vec{\mathrm{D}}$ field is continuous at the vacuum-gold interface, the transmitted polarization right under the gold surface is proportional to the sum of the incident and reflected field.

The aspect ratio of the minor to the major axis of the polarization ellipse is $r = 0.45$. When projected on the gold surface this ratio is only $r_{xy} = 0.20$, much closer to linear than to circular polarization. The elliptical polarization can be expressed as a sum of left- and right-circular polarizations with (non-normalized) amplitudes $\mathrm{E}_{\mathrm{right-circ.}} = 1$ and $\mathrm{E}_{\mathrm{left-circ.}} = 1 - r$ (and vice-versa for the opposite polarizations). As a result, we expect that the spin-polarization of the photoexcited electrons is reduced by $(\mathrm{E}_{\mathrm{right-circ.}} - \mathrm{E}_{\mathrm{left-circ.}})/(\mathrm{E}_{\mathrm{right-circ.}} + \mathrm{E}_{\mathrm{left-circ.}}) = r/(2 - r)$. Thus, for $r = 0.45$ we expect a reduction factor of the spin-polarization of 0.29 and for the ellipticity projected on the gold surface of $r_{xy} = 0.20$ a reduction factor of 0.11.

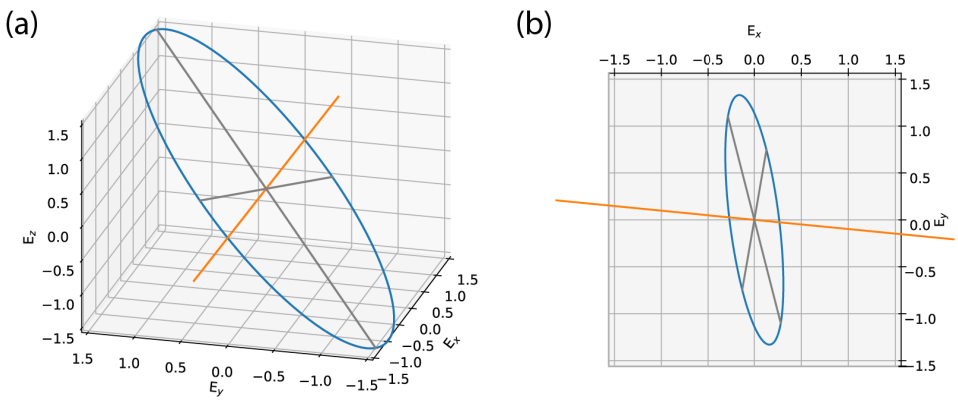

Figure 6.11: Three-dimensional view (a) and top view (b; i.e., projected on the gold surface) of the light polarization (electric field vector, blue) at the gold surface. The major/minor axes of the ellipse (gray) and the normal (orange) are shown for orientation. The reflected light experiences a phase shift difference between s- and p-polarization and is superimposed on the incoming light.

If we assume that the polarization transmitted into the gold surface is decisive for the photoemitted spin-polarization, the off-normal light incidence in our experiment diminishes the detectable spin population asymmetry by a factor nine, making a CISS-related intensity difference of 10% indistinguishable from the spatial variation of incident polarization. This may be improved by optimizing the elliptical polarization of the incident light.

6.3 Conclusions and Recommendations

While the optical polarization is well characterized in our experiment, the quality of the chiral layer prevents us from making final claims about the CISS effect in BINAP. Specifically, Ray et al. [1] showed that little disorder (1% of the opposite enantiomer) destroys the spin selectivity of the sample. Measurements of the flatness of the molecular film and the depth of the scratched trench show that we did not have a self-assembled monolayer. To grow better films, more elaborate characterization techniques, e.g., ellipsometry, are necessary. When imaging polarization-dependent photoemission we recommend having a known-achiral reference area, to be contrasted to the signal.

While we have aligned the polarizers to yield symmetric photoemission on the beam spot on the electron-optical axis, the other areas show streak-like asymmetries of up to 1%. These asymmetries do not correlate with the features on the sample and are thus attributed to the illumination optics. Together with the off-normal incidence, reducing the spin-polarization of the electrons photoemitted from the gold surface by up to a factor nine, this asymmetry is comparable to the asymmetry in photoemission due to the CISS effect, which is in the order of 10% as suggested in [5,10] (at normal incidence of circularly polarized light). The effect of asymmetric polarization of the incident light may be partially mitigated by patterning achiral reference areas on the sample on a length scale much smaller than the streaks seen in the illumination.

The experiment could be improved by aligning the illumination laser to perpendicular incidence, thus removing the asymmetry between s- and p-linearly polarized light. In a LEEM setup, this would require aligning the laser beam through the electromagnetic prism and through the electromagnetic objective lens. Alternatively, it is more feasible to reach normal light incidence by illuminating the sample from the backside. This requires a gold surface grown on a transparent, optically isotropic substrate (at UV wavelengths) and polarization-controlled illumination from the back of the sample holder. After we conducted the above experiments, a back illumination of the sample holder was installed in our LEEM instrument to conduct back-illuminated PEEM [26]. In the final form of optical near-field electron microscopy (ONEM) [27] polarization control will be added to the ESCHER LEEM, fulfilling the requirements for new photoemission experiments on chiral organic layers with a more suitable illumination geometry.

We note that spin-dependent low energy electron microscopy (SPLEEM) [28] and angle-resolved photoemission spectroscopy (ARPES, spin-PES) [29,30] setups are developed, that can gain insight into the CISS effect with spatial and angular resolution in the future.

The variety of measurement techniques that have shown the CISS effect also implies that the effect is robust over a large energy scale. While the transport experiments probe the band structure around the Fermi energy, the photoemission experiments (together with time-of-flight spectroscopy) reveal it up to 2 eV above the vacuum level, i.e., 5 to 8 eV higher. This energy scale is in practice limited by the photon energy that can be applied without damaging the sample.

The robustness in applications and the implications for the understanding of biological chiral molecules make the study of chirality-induced effects fascinating and worthwhile. Despite the large progress in recent years, it still requires efforts from experimental and theoretical side to fully understand the CISS effect.

Acknowledgements

We acknowledge Brenda Rovers for fabricating the plasmonic samples and the first organic layer samples, and Chunwei Hsu, Ferdinand Grozema and Abbey Philip for providing us with the modified BINAP molecule. We thank the groups of Jan van Ruitenbeek, Ferdinand Grozema, Herre van der Zant, and Jos Thijssen for valuable discussions throughout the project.

References

[1] K. Ray, S.P. Ananthavel, D.H. Waldeck, R. Naaman, Asymmetric scattering of polarized electrons by organized organic films of chiral molecules, Science (80-.). 283 (1999) 814–816. https://doi.org/10.1126/science.283.5403.814.

[2] F. Evers, A. Aharony, N. Bar-Gill, O. Entin-Wohlman, P. Hedegård, O. Hod, P. Jelinek, G. Kamieniarz, M. Lemeshko, K. Michaeli, V. Mujica, R. Naaman, Y. Paltiel, S. Refaely-Abramson, O. Tal, J. Thijssen, M. Thoss, J.M. van Ruitenbeek, L. Venkataraman, D.H. Waldeck, B. Yan, L. Kronik, Theory of Chirality Induced Spin Selectivity: Progress and Challenges, Adv. Mater. 34 (2022) 1–11. https://doi.org/10.1002/adma.202106629.

[3] T.K. Das, F. Tassinari, R. Naaman, J. Fransson, Temperature-Dependent Chiral-Induced Spin Selectivity Effect: Experiments and Theory, J. Phys. Chem. C 126 (2022) 3257–3264. https://doi.org/10.1021/acs.jpcc.1c10550.

[4] J.M. van Ruitenbeek, R. Korytár, F. Evers, Chirality-controlled spin scattering through quantum interference, J. Chem. Phys. 159 (2023). https://doi.org/10.1063/5.0156316.

[5] B. Göhler, V. Hamelbeck, T.Z. Markus, M. Kettner, G.F. Hanne, Z. Vager, R. Naaman, H. Zacharias, Spin selectivity in electron transmission through self-assembled monolayers of double-stranded DNA - Supplementary Information, Science (80-.). 331 (2011) 894–897. https://doi.org/10.1126/science.1199339.

[6] Z. Xie, T.Z. Markus, S.R. Cohen, Z. Vager, R. Gutierrez, R. Naaman, Spin specific electron conduction through DNA oligomers, Nano Lett. 11 (2011) 4652–4655. https://doi.org/10.1021/nl2021637.

[7] V. Kiran, S.P. Mathew, S.R. Cohen, I. Hernández Delgado, J. Lacour, R. Naaman, Helicenes - A New Class of Organic Spin Filter, Adv. Mater. 28 (2016) 1957–1962. https://doi.org/10.1002/adma.201504725.

[8] D. Amsallem, A. Kumar, R. Naaman, O. Gidron, Spin polarization through axially chiral linkers: Length dependence and correlation with the dissymmetry factor, Chirality 35 (2023) 562–568. https://doi.org/10.1002/chir.23556.

[9] C. Clever, E. Wierzbinski, B.P. Bloom, Y. Lu, H.M. Grimm, S.R. Rao, W.S. Horne, D.H. Waldeck, Benchmarking Chiral Induced Spin Selectivity Measurements - Towards Meaningful Comparisons of Chiral Biomolecule Spin Polarizations, Isr. J. Chem. 62 (2022) 1–14. https://doi.org/10.1002/ijch.202200045.

[10] M. Kettner, V. V. Maslyuk, D. Nürenberg, J. Seibel, R. Gutierrez, G. Cuniberti, K.H. Ernst, H. Zacharias, Chirality-Dependent Electron Spin Filtering by Molecular Monolayers of Helicenes, J. Phys. Chem. Lett. 9 (2018) 2025–2030. https://doi.org/10.1021/acs.jpclett.8b00208.

[11] E. Hecht, 4 The Propagation of Light, in: Optics, 2nd ed., Addison-Wesley Publishing Company, 1987.

[12] D.E. Aspnes, A.A. Studna, Dielectric functions and optical parameters of Si, Ge, GaP, GaAs, GaSb, InP, InAs, and InSb from 1.5 to 6.0 eV, Phys. Rev. B 27 (1983) 985–1009. https://doi.org/10.1103/PhysRevB.27.985.

[13] A. Ciesielski, L. Skowronski, M. Trzcinski, E. Górecka, P. Trautman, T. Szoplik, Evidence of germanium segregation in gold thin films, Surf. Sci. 674 (2018) 73–78. https://doi.org/10.1016/j.susc.2018.03.020.

[14] W.M. Haynes, CRC Handbook of Chemistry and Physics, CRC Press, 2014. https://doi.org/10.1201/b17118.

[15] W.M.H. Sachtler, G.J.H. Dorgelo, A.A. Holscher, The work function of gold, Surf. Sci. 5 (1966) 221–229. https://doi.org/10.1016/0039-6028(66)90083-5.

[16] A.N. Guerreiro, I.B. Costa, A.B. Vale, M.H. Braga, Distinctive Electric Properties of Group 14 Oxides: SiO2, SiO, and SnO2, Int. J. Mol. Sci. 24 (2023). https://doi.org/10.3390/ijms242115985.

[17] T. Yoshioka, H. Fujita, Y. Kimura, Y. Hattori, M. Kitamura, Wide-range work function tuning in gold surfaces modified with fluorobenzenethiols toward application to organic thin-film transistors, Flex. Print. Electron. 5 (2020). https://doi.org/10.1088/2058-8585/ab71e3.

[18] Q. Sun, K. Ueno, H. Yu, A. Kubo, Y. Matsuo, H. Misawa, Direct imaging of the near field and dynamics of surface plasmon resonance on gold nanostructures using photoemission electron microscopy, (2013) 1–8. https://doi.org/10.1038/lsa.2013.74.

[19] C. Hsu, Chirality-induced spin selectivity, in: Conform. Spin Eff. Single - Mol. Electron. Transp., 2022: pp. 99–121. https://doi.org/10.4233/uuid:1d3b6977-0abf-40fa-bc94-b7617e158b81.

[20] F.L. Pedrotti, L.S. Pedrotti, L.M. Pedrotti, 14 Matrix treatment of Polarization, in: Introd. to Opt., 2nd ed., Pearson Prentice Hall, San Francisco, 1993.

[21] E. Hecht, A. Zajac, 8 Polarization, in: Optics, 4th ed., Addison-Wesley Publishing Company, 1979. https://books.google.nl/books?id=eLruAAAAMAAJ.

[22] A. Tebyani, F.B. Baalbergen, R.M. Tromp, S.J. van der Molen, Low-Energy Electron Irradiation Damage in Few-Monolayer Pentacene Films, J. Phys. Chem. C 125 (2021) 26150–26156. https://doi.org/10.1021/acs.jpcc.1c06749.

[23] T. Liu, X. Wang, H. Wang, G. Shi, F. Gao, H. Feng, H. Deng, L. Hu, E. Lochner, P. Schlottmann, S. Von Molnár, Y. Li, J. Zhao, P. Xiong, Linear and nonlinear two-terminal spin-valve effect from chirality-induced spin selectivity, ACS Nano 14 (2020) 15983–15991. https://doi.org/10.1021/acsnano.0c07438.

[24] A. Steinbacher, P. Nuernberger, T. Brixner, Optical discrimination of racemic from achiral solutions, Phys. Chem. Chem. Phys. 17 (2015) 6340–6346. https://doi.org/10.1039/c4cp05641h.

[25] F.A. Jenkins, H.E. White, Chapter 25: Reflection, in: Fundam. Opt., 4th ed, 1976: pp. 523–543.

[26] A. Moradi, M. Rog, G. Stam, R.M. Tromp, S.J. van der Molen, Back illuminated photo emission electron microscopy (BIPEEM), Ultramicroscopy 253 (2023) 113809. https://doi.org/https://doi.org/10.1016/j.ultramic.2023.113809.

[27] R. Marchand, R. Šachl, M. Kalbáč, M. Hof, R. Tromp, M. Amaro, S.J. Van Der Molen, T. Juffmann, Optical Near-Field Electron Microscopy, Phys. Rev. Appl. 16 (2021) 1–8. https://doi.org/10.1103/PhysRevApplied.16.014008.

[28] L. Yu, W. Wan, T. Koshikawa, M. Li, X. Yang, C. Zheng, M. Suzuki, T. Yasue, X. Jin, Y. Takeda, R. Tromp, W.X. Tang, Aberration corrected spin polarized low energy electron microscope, Ultramicroscopy 216 (2020) 113017. https://doi.org/10.1016/j.ultramic.2020.113017.

[29] C. Jozwiak, J.A. Sobota, K. Gotlieb, A.F. Kemper, C.R. Rotundu, R.J. Birgeneau, Z. Hussain, D.H. Lee, Z.X. Shen, A. Lanzara, Spin-polarized surface resonances accompanying topological surface state formation, Nat. Commun. 7 (2016) 1–7. https://doi.org/10.1038/ncomms13143.

[30] Y.S. Dedkov, M. Fonin, U. Rüdiger, G. Güntherodt, Spin-resolved photoelectron spectroscopy of the MgO/Fe(110) system, Appl. Phys. A 82 (2006) 489–493. https://doi.org/10.1007/s00339-005-3447-2.